Cellular/Molecular

CaMKII Drives Synaptic Maturation by Coordinating Spine Remodeling and Receptor Segregation via Liquid–Liquid Phase Separation

Leah Men Shin Kuo,[1] Pin-Wu Liu,[1] Misa Arizono,[1,2] and Yasunori Hayashi[1]
[1]Department of Pharmacology, Kyoto University Graduate School of Medicine, Kyoto 606-8501, Japan and [2]The Hakubi Center for Advanced Research, Kyoto University, Kyoto 606-8501, Japan

A hallmark of mature excitatory synapses is their localization on dendritic spines, which increase in number and enlarge during development. Recent super-resolution studies have uncovered another key feature of mature synapses—an intricate synaptic nanoarchitecture. Trans-synaptic nanocolumns align AMPA-type glutamate receptor (AMPAR) nanodomains with presynaptic release sites, ensuring efficient synaptic transmission as neurons mature. However, the mechanism by which these key features of synaptic maturation emerge remains unclear. Ca^{2+}/calmodulin-dependent protein kinase II (CaMKII) is a signaling molecule implicated in regulating excitatory synaptic transmission. Recent findings show CaMKII, beyond its function as a kinase, serves as a structural element through its ability to undergo liquid–liquid phase separation (LLPS). Upon activation in vitro, it segregates AMPAR from NMDA-type glutamate receptors (NMDAR), forming biphasic condensates. Given that CaMKII expression increases during development, we hypothesized that it serves as the driving force behind synaptic maturation. Using super-resolution microscopy and primary hippocampal cultures prepared from embryonic rat pups of both sexes, we found that immature neurons, which express lower levels of CaMKII, exhibit smaller spine density and size and less-developed AMPAR and NMDAR nanodomain segregation compared with mature neurons. Remarkably, overexpressing CaMKII in immature neurons was sufficient to recapitulate the features of mature synapses, by increasing spine density, size, and receptor nanodomain segregation. Conversely, a single CaMKII mutation (I205K), which prevents LLPS, abolished these effects. Our findings support that CaMKII-mediated LLPS is the driving force shaping the mature synaptic landscape, suggesting a previously overlooked mechanistic link between dendritic spine formation, enlargement, and receptor nanodomain organization.

Key words: AMPA-type glutamate receptor; Ca^{2+}/calmodulin-dependent protein kinase II (CaMKII); liquid–liquid phase separation; NMDA-type glutamate receptor; super-resolution microscopy; synapse

Significance Statement

Mature excitatory synapses exhibit several defining features, including high dendritic spine density, large dendritic spine heads, and the presence of trans-synaptic nanocolumns that align AMPA-type glutamate receptors with presynaptic release sites. However, the mechanisms driving the emergence of this mature synaptic architecture remain poorly understood. Using super-resolution microscopy, we found that Ca^{2+}/calmodulin-dependent protein kinase II (CaMKII), via liquid–liquid phase separation (LLPS), can single-handedly drive the maturation of synapses from an immature state. These findings highlight a pivotal role of CaMKII-mediated LLPS in synaptic maturation.

Received May 2, 2025; revised Sept. 26, 2025; accepted Oct. 10, 2025.

Author contributions: L.M.S.K., P.-W.L., M.A., and Y.H. designed research; L.M.S.K. performed research; L.M.S.K. analyzed data; L.M.S.K., P.-W.L., M.A., and Y.H. wrote the paper.

We thank Dr. Takeo Saneyoshi for providing DNA constructs, Dr. Eric Gouaux for the antibodies used in this study, Dr. Hanna Zieger for the advice on dSTORM experiments, and Dr. Nozomi Asaoka for the comments on statistical analysis. L.M.S.K. was supported by the Graduate Program for Medical Innovation, Kyoto University. This work was supported by Grant-in-Aid for Scientific Research JP18H05434, JP20K21462, and JP22K21353; from the MEXT, The Uehara Memorial Foundation, The Naito Foundation, Research Foundation for Opto-Science and Technology, Novartis Foundation, and The Takeda Science Foundation, HFSP Research Grant RGP0020/2019, JST CREST JPMJCR20E4, and AMED Grants JP24zf0127010 and JP25wm0625123h0002 to Y.H.; by Grant-in-Aid for Scientific Research JP22K18372, from the MEXT and JST FOREST JPMJFR2141 and Brain Science Foundation to M.A.; and by Grant-in-Aid for Research Activity Start-up (JP24K23243) from JSPS, Narishige Neuroscience Research Foundation, Konica Minolta Science and Technology Foundation, and Hirose Foundation to P.-W.L.

The authors declare no competing financial interests.

Correspondence should be addressed to Misa Arizono at arizono.misa.7s@kyoto-u.ac.jp or Yasunori Hayashi at yhayashi-tky@umin.ac.jp.

https://doi.org/10.1523/JNEUROSCI.0871-25.2025

Introduction

Synaptic maturation is a fundamental process that shapes neuronal circuits during development and throughout adulthood, where synapses undergo continuous remodeling. This maturation involves two key aspects: (1) structural changes in the number and morphology of synapses and (2) molecular regulations in their composition and distribution. In immature neurons, excitatory synapses are directly formed on the dendritic shaft. The neurons gain dendritic spines as they mature, where synapses are predominantly formed. Synapses increase in the number and size during maturation while undergoing pruning to refine functional networks. Importantly, such process is accompanied by molecular reorganization of neurotransmitter receptors, scaffolding proteins, and regulatory molecules that establish intricate synaptic machinery. Recent studies have identified a specialized structure that coordinates postsynaptic organization with presynaptic neurotransmitter release, ensuring efficient synaptic transmission (Tang et al., 2016; Biederer et al., 2017; Hruska et al., 2018; Martinez-Sanchez et al., 2021). This so-called trans-synaptic nanocolumn aligns AMPA-type glutamate receptor (AMPAR) nanodomains directly beneath presynaptic release sites, reflecting a remarkable sophistication of synaptic nanoarchitecture. Despite its significance, how this structure forms and whether it is linked to dendritic spine growth remains unclear.

Ca^{2+}/calmodulin-dependent protein kinase II (CaMKII), a key postsynaptic density protein plays a central role in structural plasticity, learning, and memory (Kim et al., 2016; Yasuda et al., 2022). Upon Ca^{2+} influx through NMDA-type glutamate receptors (NMDARs), CaMKII activation triggers pathways that drive spine enlargement and synaptic strengthening. Behind its well-established role in structural remodeling, we recently proposed that CaMKII also shapes synaptic molecular organization by promoting the formation of nanodomains and nanocolumns via liquid–liquid phase separation (LLPS; Hosokawa et al., 2021; Liu et al., 2021). In vitro experiments revealed that CaMKII undergoes LLPS with the carboxyl tail of the NMDAR subunit GluN2B upon Ca^{2+}/calmodulin stimulation, forming stable condensates even after Ca^{2+} removal—potentially mimicking the conversion of transient Ca^{2+} signals into long-lasting synaptic modifications (Cai et al., 2021; Hosokawa et al., 2021). Further experiments incorporating the AMPAR auxiliary subunit stargazin, neuroligin, and the scaffolding protein PSD-95 demonstrated a phase-in-phase assembly, where stargazin, neuroligin, and PSD-95 formed an inner phase, while CaMKII and GluN2B constituted an outer phase (Hosokawa et al., 2021). This organization may explain how nanocolumn-associated proteins, such as AMPARs, are concentrated and maintained. Indeed, we found that disrupting CaMKII-mediated condensates in neurons reduced AMPAR/neuroligin and NMDAR nanodomain segregation (Hosokawa et al., 2021). These findings suggest that CaMKII-driven LLPS contributes to shaping synaptic nanoarchitecture, including the formation of trans-synaptic nanocolumns. Combined with the fact that CaMKII expression increases during development (Kelly et al., 1987; Fink et al., 2003; Li et al., 2003), we hypothesized that CaMKII serves as a coordinator that drives both morphological changes of the dendritic spine and trans-synaptic nanocolumn formation required for synaptic maturation.

Using direct stochastic optical reconstruction microscopy (dSTORM), we investigated the nanoscale organization of AMPARs and NMDARs alongside structural changes in dendritic spines during neuronal development and examined the role of CaMKII in shaping the mature synaptic landscape. Our findings reveal that immature neurons, which have lower CaMKII expression, exhibit fewer dendritic spines with smaller head areas and less segregation between AMPAR and NMDAR nanodomains compared with mature neurons. Notably, overexpressing CaMKII in immature neurons was sufficient to drive dendritic spine formation and enlargement, as well as to enhance AMPAR and NMDAR nanodomain segregation to levels observed in mature neurons. Conversely, a single-point mutation in CaMKII (I205K), which makes CaMKII unable to bind to GluN2B and disrupts LLPS, abolished not only the segregation effect but also the structural changes of dendritic spines. These results highlight the critical role of CaMKII expression levels in synaptic nanoarchitecture development and underscore the central role of CaMKII-mediated LLPS in orchestrating dendritic spine formation, enlargement, and receptor nanodomain organization to establish the mature synaptic landscape.

Materials and Methods

DNA constructs. GFP-CaMKIIα was provided by Dr. Takeo Saneyoshi (Institute of Science Tokyo). Specifically, the full-length human CaMKIIα cDNA was isolated from human hippocampal cDNA (Clontech Laboratories) and subcloned into pDEST201, a Gateway donor vector. It was then further subcloned into the pCAGGS-Gateway-mGFP vector, resulting in an N-terminal, in-frame mGFP tag on CaMKIIα. Site-directed mutagenesis of the GFP-CaMKIIα (I205K) mutant was performed using an inverse PCR-based method.

Neuronal culture and transfection. All experiments were carried out conforming to the ethical and safety standards of the Kyoto University Animal Experiments Committee. Banker-type hippocampal neurons were obtained from Embryonic Day 18 (E18) Sprague Dawley rats of both sexes and prepared according to the protocol (Kaech and Banker, 2006). Hippocampi were trypsinized and plated at a density of 50,000 cells per well on 18 mm poly-L-lysine (1 mg/ml)-coated glass coverslips. Coverslips were placed over a glial feeder layer in a 12-well plate. Five micrometer cytosine arabinoside was added at days in vitro (DIV)3 to inhibit glial proliferation. Cultures were kept at 37°C with 5% CO_2/95% air.

Neurons were transfected with GFP, GFP-CaMKIIα, or GFP-CaMKIIα I205K using Lipofectamine 2000 (11668019, Thermo Fisher Scientific) between DIV7 and DIV13 and used for experiments 2–7 d after transfection. All experiments were repeated with three or more independent cultures.

Immunoblotting. Neurons from four coverslips at different DIV were rinsed with phosphate-buffered saline (PBS). Cells were scraped off and lysed in 200 µl of sodium dodecyl sulfate (SDS)-PAGE loading buffer (0.25 M Tris–HCl, 40% glycerol, 8% SDS, 20% 2-mercaptoethanol, 0.002% bromophenol blue), pH 6.8, and then centrifuged at 10,000 × *g* for 5 min. Samples were heated at 95°C for 10 min. Twenty-five microliter of the extract was separated using 10% SDS-PAGE gels and then transferred onto methanol activated polyvinylidene fluoride membranes. The membranes were blocked with 5% skimmed milk (31149-75, Nacalai Tesque) in Tris-buffered saline with 0.05% Tween-20 (TBS-T; 35624-15, Nacalai Tesque) for 1 h at room temperature. Membranes were incubated overnight at 4°C with primary antibodies: CaMKIIα 6G9 (1:500, sc-32288, Santa Cruz Biotechnology) and β-actin (1:1,000, 20535-1-AP, Proteintech). Membranes were washed between and after antibody incubations with TBS-T. Membranes were incubated with peroxidase-conjugated secondary antibodies: anti-mouse IgG (Na931V, Cytiva) and anti-rabbit IgG (Na934V, Cytiva) for 1 h at room temperature. Proteins were detected with Chemi-Lumi One Super (02230-30, Nacalai Tesque) and imaged using ChemiDoc imaging system (Bio-Rad Laboratories). Band intensity was quantified with ImageJ.

Immunostaining. For AMPAR and NMDAR, surface endogenous receptors were live stained in the 37°C incubator for 15 min using

antibodies provided by E. Gouaux that target the extracellular domains of receptors: anti-GluA2 IgG1 clone 15F1 (1:300), anti-GluA2 IgG2b clone 14B11 (1:300), and anti-GluN1 IgG1 clone 10B11 (1:300). Two different GluA2 antibodies were used because of cross-reactivity with other costained antibodies (RIM1/2 or GluN1). The cells were then fixed with 4% paraformaldehyde (PFA) and 4% sucrose in PBS at room temperature for 10 min. The cells were washed with 50 mM NH_4Cl in PBS (PBS/NH_4Cl) for five times and then treated with blocking solution [1.5% bovine serum albumin (01860-36, Nacalai Tesque), 0.1% fish gelatin, 0.1% Triton X-100 in PBS/NH_4Cl] at room temperature for 40 min. For RIM1/2 and CaMKIIα staining, the cells were permeabilized with Triton X-100 for 10 min. at room temperature and then immunolabeled with antibodies against RIM1/2 (1:500, 140205, Synaptic Systems) or CaMKIIα 6G9 (1:500) for 1 h at room temperature. After washing, cells were then incubated for 30 min at room temperature with secondary antibodies: goat anti-mouse IgG2b Alexa Fluor 647 (1:500, A21242, Thermo Fisher Scientific) for anti-GluA2 IgG2b clone 14B11, goat anti-mouse IgG1 CF568 (1:500, 20802, Biotium) for anti-GluN1 clone 10B11 and anti-GluA2 clone 15F1, goat anti-guinea pig IgG Alexa Fluor 647 (1:500, A21450, Thermo Fisher Scientific) for RIM1/2, or goat anti-mouse IgG Alexa Fluor 568 (1:500, A11031, Thermo Fisher Scientific) for CaMKIIα. After five washes, a second PFA fixation step was performed to avoid antibody detaching. Cells were imaged within 2 weeks of immunostaining.

Confocal imaging. Confocal imaging for CaMKIIα immunostaining was performed with the Nikon AX confocal system. Coverslips were placed in an imaging chamber with PBS to stop the sample from drying out. *Z*-stack images (field of view, 58.88 × 58.88 µm; pixel size, 115 nm; *z* plane 0.4 µm; 16 planes) were obtained using a Nikon 100×/1.40 oil Plan Apo objective and Nikon AX LUA-S4 lasers 488 nm (GFP) and 560 nm (CaMKIIα). *Z*-stacks were converted to maximum intensity projection images using FIJI/ImageJ. Neurons were manually traced based on GFP images (morphological marker). The mean fluorescence intensity of CaMKII signal in the traced area was measured followed by background subtraction.

dSTORM imaging. dSTORM imaging was performed for RIM1/2, AMPAR, and NMDAR immunostaining. dSTORM glucose oxidase-based STORM buffer (Beghin et al., 2017) was prepared containing 1 M Tris–HCl, pH 7.5, 10 µg/ml catalase (C3515, Sigma-Aldrich), 1 M KCl, 10% glucose, 1 mg/ml glucose oxidase (G2133-10, Sigma-Aldrich), and 1 mM cysteamine (M6500, Sigma-Aldrich). Samples were first incubated with multicolor fluorescent microspheres (TetraSpeck, T7279, Thermo Fisher Scientific), which were used as fiducial markers for lateral drift correction. Samples were placed in an imaging chamber, and 1.3 ml of STORM buffer was added. A plastic lid was placed on top to avoid oxygen exchange with ambient air. 2D STORM imaging was performed on a Nikon N-STORM super-resolution system equipped with a Nikon 100×/1.40 oil Plan Apo objective, iXon X3 EMCCD camera (Andor Technology), and fiber-coupled laser launch (405, 561, and 647 nm). Wide-field epifluorescence images of GFP signal (morphological marker) were taken before dSTORM imaging. dSTORM imaging was performed with a 20 ms exposure time, 20,000 frames per color (field of view, 15.36 × 15.36 µm; pixel size, 160 nm). Imaging using the 647 nm laser was performed prior to imaging using the 561 nm laser. The UV light 405 nm laser was used to enhance blinking.

Nanodomain analysis. Intensity-based drift-corrected dSTORM images (25 nm per pixel) were reconstructed from single-molecule localizations with PALMTracer (Kechkar et al., 2013) as a plugin software of MetaMorph (Molecular Devices; Fig. 1*B*). Nanodomains were analyzed using the SR-Tesseler method, which is based on Voronoi tessellation (Levet et al., 2015; Fig. 1*B*). Clusters were segmented by applying a threshold of twice the average density of the dataset (two minimum area × 10^4 nm^2, five minimum number of localizations). Nanodomains

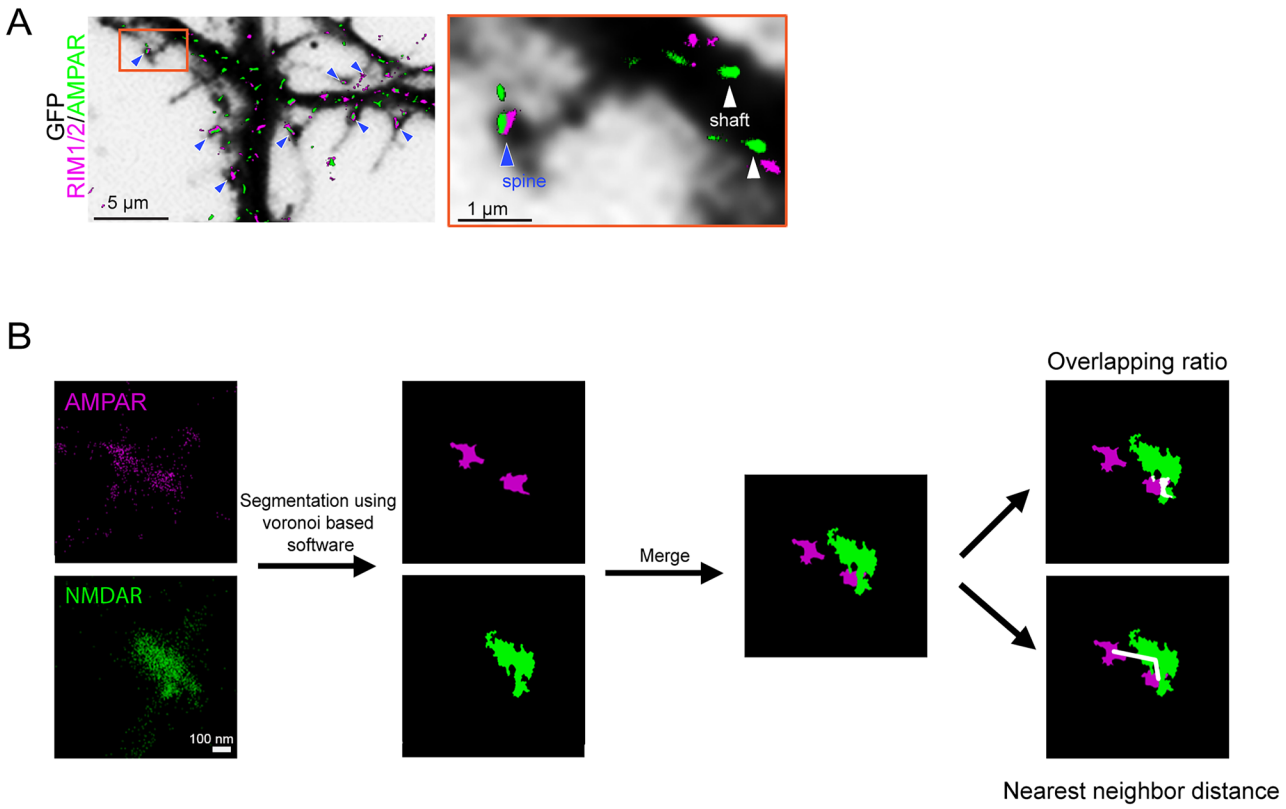

Figure 1. ROI selection and nanodomain analysis. ***A***, Inverted GFP images overlaid with RIM1/2 and AMPAR dSTORM images. Dendritic spines are shown as blue arrowheads. In the magnified image, blue arrowhead and white arrowheads represent (s) AMPAR and RIM1/2 nanodomains in dendritic spines and on the shaft respectively. ***B***, Raw dSTORM localization data was processed with SR-Tesseler, a tessellation-based software to define nanodomains. AMPAR and NMDAR were merged and nanodomain segregation was calculated using overlap (shown in white) or nearest neighbor distance (white lines).

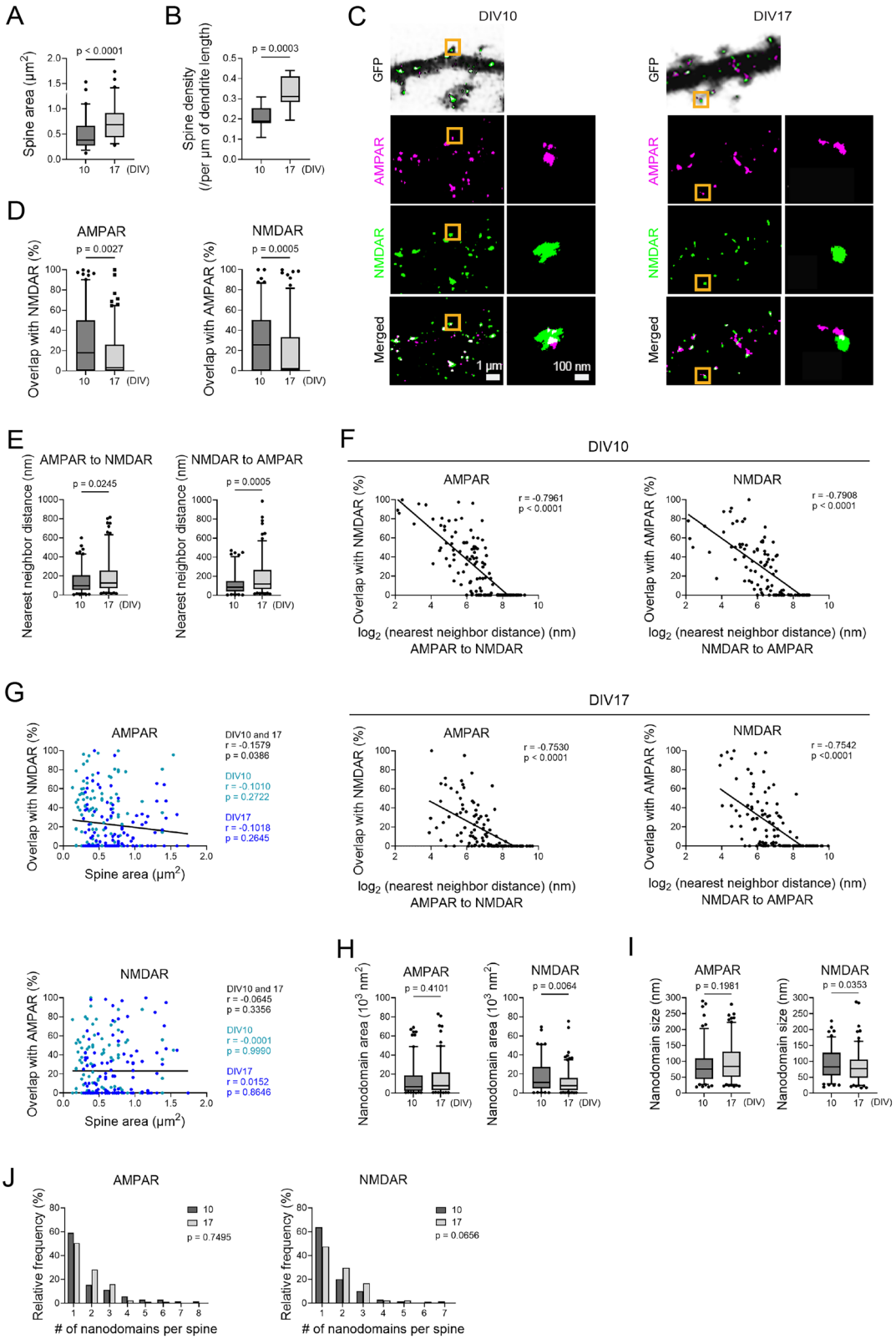

Figure 2. Glutamate receptor organization and spine remodeling during development. ***A***, The dendritic spine area in DIV10 and DIV17 neurons (Mann–Whitney *U* test, $U = 1{,}202$). $n = 61$ spines for DIV10, 73 spines for DIV17 neurons. ***B***, Dendritic spine density in DIV10 and DIV17 neurons (Mann–Whitney *U* test, $U = 12$). $n = 14$ neurons for DIV10, 10 neurons for DIV17. ***C***, Top row, Inverted GFP channel images of DIV10 and DIV17 dendrites overlaid with merged dSTORM images of AMPAR and NMDAR nanodomains. Bottom three rows, dSTORM images of dendrite (left). The orange box shows the example spine that is magnified on the right. White indicates the overlap between AMPAR and NMDAR. ***D***, Proportion of the AMPAR nanodomain area overlapping with the NMDAR nanodomain area (left, Mann–Whitney *U* test, $U = 7{,}944$) and proportion of the NMDAR nanodomain area overlapping with AMPAR nanodomain area (right, Mann–Whitney *U* test, $U = 6{,}250$) in DIV10 or DIV17 neurons. ***E***, Distance between the center of AMPAR nanodomain to the center of the nearest NMDAR nanodomain (left, Mann–Whitney *U* test, $U = 8{,}398$) and distance between the center of NMDAR nanodomain to the center of the nearest AMPAR nanodomain (right, Mann–Whitney *U* test, $U = 6{,}353$) in DIV10 and DIV17 neurons. ***F***, Correlation between nearest neighbor distance and overlapping ratio. AMPAR overlapping with NMDAR and nearest neighbor distance from AMPAR to

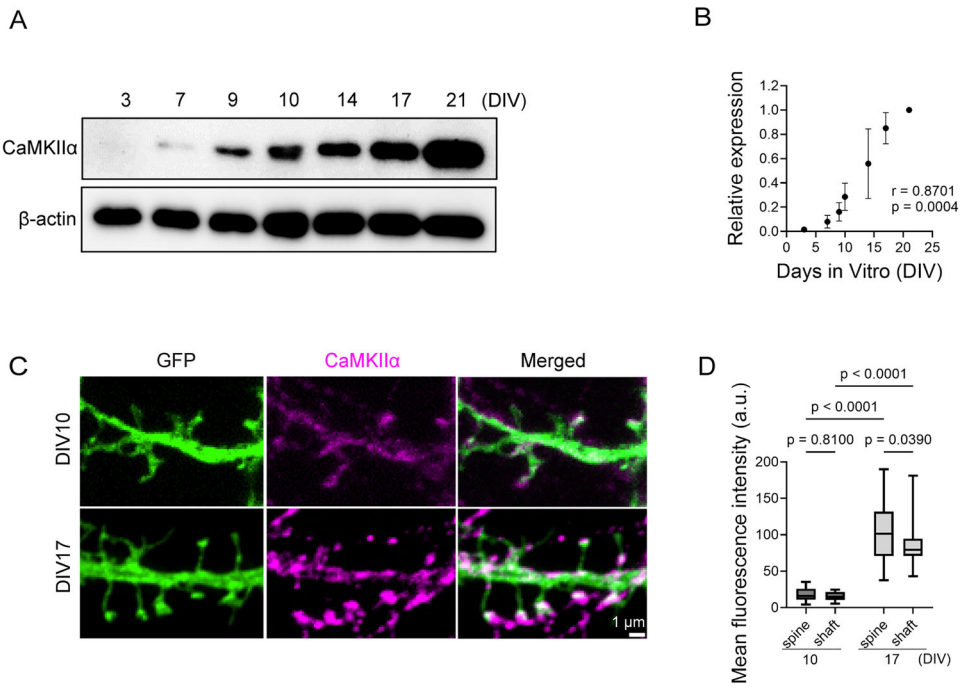

Figure 3. CaMKIIα expression increases with development. ***A***, Western blot of CaMKIIα and β-actin throughout development in Banker-type culture. ***B***, Correlation between DIV and CaMKIIα expression levels (Spearman's *R* test). CaMKIIα signals were normalized against β-actin signals and further divided by the value at DIV21. Older DIV was associated with higher CaMKIIα expression levels. $n = 3$ independent cultures. Data are represented as mean ± SEM. ***C***, Immunostaining of endogenous CaMKIIα in DIV10 and DIV17 neurons. ***D***, CaMKIIα expression in the spines and shaft of DIV10 and DIV17 neurons (two-way ANOVA, spine vs shaft, $F_{(1,58)} = 2.841$; $p = 0.0973$; DIV10 vs DIV17, $F_{(1,58)} = 123.9$; $p < 0.0001$; interaction, $F_{(1,58)} = 1.821$; $p = 0.1824$; Fisher's LSD test). ROIs were manually drawn over the shaft and spines using GFP images as reference. $n = 16$ cells for DIV10, 18 cells for DIV17 from at least three independent cultures.

were segmented by applying a threshold of one time the average density of each cluster (0.01×10^4 nm^2 minimum area, 50 minimum number of localizations). Regions of interests (ROIs) were chosen by identifying spines in a merged image of the reconstructed immunostaining images with the GFP epifluorescence image. The segregation between AMPAR and NMDAR nanodomains were calculated from the overlapping nanodomain areas (Fig. 1*B*) in ROIs. As an alternative measure of segregation, the nearest neighbor distance was determined, defined as the distance between the center of an AMPAR nanodomain and the center of the nearest NMDAR nanodomain and vice versa (Fig. 1*B*). Nanodomain sizes were defined as the average of width and length. Nanodomain sizes were calculated by principal-component analysis as detailed in Levet et al. (2015), while all other measures were calculated using the outline of the original cluster segmentation.

Statistical analysis. Data were collected from at least three independent cultures. For box plots, the center line, box, and whisker represent the median, 25th–75th percentile and 5th–95th percentile, respectively. GraphPad Prism 10 was used to perform all statistical analysis. The normality and equal variances of the datasets were tested, and the appropriate statistical tests were chosen for each dataset. Statistical significance was calculated using Mann–Whitney *U* test for comparisons between two groups. For comparisons between three groups or more, the Kruskal–Wallis test with post hoc Dunn's multiple comparisons test or two-way ANOVA with post hoc Fisher's LSD test was used. For correlations between groups, Spearman's *R* test was used. *P* values <0.05 were considered statistically significant.

Results

Segregation of AMPAR and NMDAR nanodomains increase with development

To assess how dendritic spines and the distribution of AMPAR and NMDAR nanodomains change during development, we used Banker-type hippocampal neuronal cultures, where dissociated hippocampal neurons grow on the underside of coverslips suspended above a glial feeder layer (Kaech and Banker, 2006). This approach allows for low-density, glial-free cultures, ideal for high-resolution imaging of cultured hippocampal neurons at our targeted developmental stages: DIV10, when synaptogenesis occurs, and DIV17, when synapses are considered mature (Kaech and Banker, 2006).

To investigate AMPAR and NMDAR distribution within synapses, we first identified synapses by costaining AMPAR and the presynaptic marker protein RIM1/2. After immunolabeling the surface AMPAR subunit GluA2 with an antibody against its extracellular domain, we permeabilized the cells and stained with RIM1/2 antibody. We then performed dSTORM imaging to examine synapse locations. AMPARs showed a punctate distribution throughout the cells, but not all puncta coincided with RIM1/2 signals, likely indicating extrasynaptic receptors. We classified the AMPAR puncta by their localization to either dendritic spines or shafts by visualizing the neuronal structure

←

NMDAR (left, Spearman's *R* test), NMDAR overlapping with AMPAR and nearest neighbor distance from NMDAR to AMPAR (right, Spearman's *R* test) in DIV10 (top, Spearman's *R* test) and DIV17 (bottom, Spearman's *R* test) neurons. ***G***, Correlation between the spine area and AMPAR/NMDAR overlapping ratio. AMPAR overlapping with NMDAR (top, Spearman's *R* test) and NMDAR overlapping with AMPAR (bottom, Spearman's *R* test) in DIV10 and DIV17 neurons. ***H***, The area of AMPAR (left, Mann–Whitney *U* test, $U = 9{,}511$) and NMDAR (right, Mann–Whitney *U* test, $U = 7{,}195$) nanodomains in DIV10 and DIV17 neurons. ***I***, The size of AMPAR (left, Mann–Whitney *U* test, $U = 8{,}990$) and NMDAR (right, Mann–Whitney *U* test, $U = 7{,}189$) nanodomains in DIV10 and DIV17 neurons. ***J***, The number of AMPAR (left, Mann–Whitney *U* test, $U = 2{,}797$) and NMDAR (right, Mann–Whitney *U* test, $U = 2{,}445$) nanodomains per spine in DIV10 and DIV17 neurons. The same sets of spines are used from ***C*** to ***J***. $n = 71$ spines for DIV10 from eight cells, 75 spines from eight cells for DIV17 from at least three independent cultures.

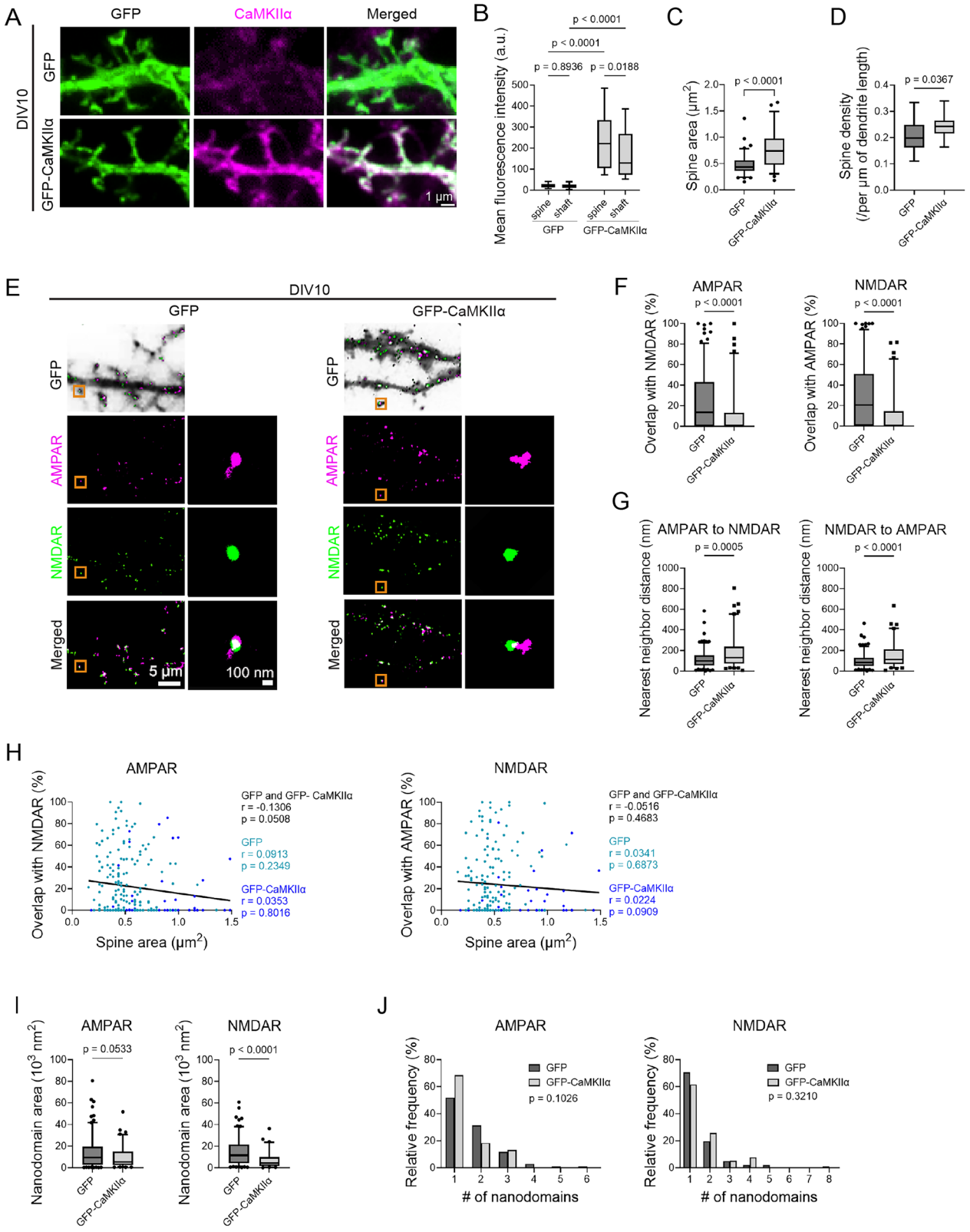

Figure 4. CaMKIIα overexpression recreates the mature synaptic landscape. ***A***, Immunostaining of CaMKIIα in GFP and GFP-CaMKIIα expressing DIV10 neurons. ***B***, CaMKIIα expression in the spines and shaft of GFP and GFP-CaMKIIα expressing neurons (two-way ANOVA, spine vs shaft, $F_{(1,68)} = 3.231$; $p = 0.0767$; GFP vs GFP-CaMKIIα, $F_{(1,68)} = 88.27$; $p < 0.0001$; interaction, $F_{(1,68)} = 2.584$; $p = 0.1126$; Fisher's LSD test). $n = 27$ cells for GFP and 21 cells for GFP-CaMKIIα expressing DIV10 neurons, from at least three independent cultures. ***C***, The dendritic spine area in GFP and GFP-CaMKIIα expressing neurons (Mann–Whitney U test, $U = 1{,}177$). $n = 86$ spines for GFP, 58 spines for GFP-CaMKIIα overexpressing neurons. ***D***, Dendritic spine density in GFP and GFP-CaMKIIα expressing neurons (Mann–Whitney U test, $U = 57$). $n = 15$ neurons for GFP and 14 neurons for GFP-CaMKIIα expressing neurons. ***E***, Top row, Inverted GFP channel image of GFP (control) and GFP-CaMKIIα overexpressing dendrites overlaid with merged dSTORM images of AMPAR and NMDAR nanodomains of the same region. Bottom three rows, dSTORM images of dendrite (left). Orange boxes show example spines magnified on the right. White indicates the overlap between AMPAR and NMDAR. ***F***, Proportion of AMPAR nanodomain area overlapping with NMDAR nanodomain area (left, Mann–Whitney U test, $U = 4{,}980$) and proportion of NMDAR nanodomain area overlapping with the AMPAR nanodomain area (right,

with cytosolic GFP. Most AMPAR puncta in dendritic spines juxtaposed RIM1/2 (30 out of 31, 97% in three neurons at DIV10), while only a subset on the shaft did (101 out of 313, 32%; Fig. 1*A*). Therefore, we focused on the signal in dendritic spines revealed by GFP.

Having identified the location of synapses, we investigated the distribution of AMPAR and NMDAR nanodomains in DIV10 and DIV17 neurons using dSTORM (Fig. 1*B*). As previously reported (Papa et al., 1995), we observed an increase in the dendritic spine size and density during this period (Fig. 2*A*,*B*). Using antibodies against the extracellular domains of the AMPAR subunit GluA2 and the NMDAR subunit GluN1, we immunolabeled surface AMPARs and NMDARs and analyzed the overlap between their nanodomains. We observed a significant increase in segregation (i.e., reduced overlap; Fig. 1*B*) between AMPAR and NMDAR nanodomains in DIV17 compared with DIV10 (Fig. 2*C*,*D*). The nearest neighbor distance between AMPAR and NMDAR nanodomains (Fig. 1*B*), which also reflects the degree of segregation, significantly increased at DIV17 (Fig. 2*E*). These two parameters showed a strong correlation, supporting the validity of the measurements (Fig. 2*F*). Although both the spine size and AMPAR/NMDAR segregation increased during development, the spine size itself did not correlate with the overlapping ratio (Fig. 2*G*). There were no significant differences in the AMPAR nanodomain area, size, or number (Fig. 2*H–J*) between DIV10 and DIV17. The NMDAR nanodomain area and size (Fig. 2*H*,*I*) decreased in DIV17 neurons, while the number of nanodomains per spine remained unchanged (Fig. 2*J*).

CaMKIIα expression increases with development

To investigate the developmental mechanism driving the increase in the spine size and the segregation between AMPAR and NMDAR nanodomains, we focused on CaMKII, a protein implicated in both phenomena whose expression increases during development (Kelly et al., 1987; Fink et al., 2003; Li et al., 2003). We first evaluated whether the developmental expression profile of CaMKII is maintained in Banker-type cultures. Among the various isoforms of CaMKII, CaMKIIα is the main subtype expressed in forebrain neurons and drives LLPS (Cai et al., 2021), so we concentrated on CaMKIIα. Western blot results showed that development is associated with an increase in CaMKII expression in Banker-type cultures (Fig. 3*A*,*B*), consistent with in vivo development. Immunostaining with a CaMKIIα antibody also confirmed a significant increase in CaMKIIα expression in the spines and shafts of DIV17 neurons compared with DIV10 neurons (Fig. 3*C*,*D*). Notably, at DIV17, CaMKIIα exhibited greater enrichment in spines relative to shafts.

CaMKIIα governs synapse maturation

To assess whether the change in CaMKIIα expression alone is sufficient to induce developmental changes in the synaptic landscape, we overexpressed GFP-CaMKIIα in DIV10 neurons, where endogenous CaMKIIα expression was lower than that of DIV17 (Fig. 3). Immunostaining validated effective overexpression of CaMKIIα in DIV10 neurons (Fig. 4*A*,*B*), reaching levels of DIV17 (Fig. 3*C*,*D*). Overexpressing CaMKIIα in DIV10 neurons recapitulated several key aspects of the mature synaptic landscape observed in DIV17 neurons. First, CaMKIIα overexpression increased both the spine size and density in DIV10 neurons (Fig. 4*C*,*D*). Second, we observed that CaMKIIα overexpression in DIV10 neurons led to greater segregation of AMPAR and NMDAR nanodomains (Fig. 4*E–G*). As with DIV10 and DIV17 neurons, the degree of segregation showed no correlation with the spine size (Fig. 4*H*). Third, the trends in the area and number of AMPAR and NMDAR nanodomains remained consistent, with only NMDARs exhibiting a smaller area (Fig. 4*I*,*J*). In summary, overexpressing CaMKIIα in DIV10 neurons recapitulated the key synaptic features observed in DIV17 neurons. These findings highlight the critical role of CaMKIIα in shaping the mature synaptic landscape by promoting dendritic spine formation and enlargement, as well as segregating glutamate receptor nanodomains.

CaMKIIα-mediated LLPS governs AMPAR and NMDAR nanodomain segregation

To specifically test the role of CaMKIIα-mediated LLPS in synaptic maturation, we introduced the I205K mutation into GFP-CaMKIIα, which disrupts CaMKIIα-mediated LLPS by impairing the binding between CaMKIIα and the GluN2B subunit of NMDAR (Hosokawa et al., 2021; Özden et al., 2022). GFP-CaMKIIα I205K was expressed in immature DIV10 neurons, where endogenous CaMKIIα expression was low (Fig. 3), to assess its effects on AMPAR and NMDAR nanodomain segregation. Unlike GFP-CaMKIIα WT, overexpressing GFP-CaMKIIα I205K did not induce significant changes in the segregation or area of glutamate receptor nanodomains (Fig. 5*C–F*). Consistent with our previous study, these results strongly indicate that CaMKIIα-mediated LLPS plays a significant role in glutamate receptor organization. Notably, we observed that this mutant also abolished CaMKIIα's effect on increasing spine density and head size (Fig. 5*A*,*B*), suggesting a link between LLPS and structural changes in spines, which are likely crucial for coordinated synaptic maturation.

Discussion

Using dSTORM, we examined the distribution of AMPAR and NMDAR nanodomains during development and investigated the role of CaMKIIα in shaping this distribution. We found that in immature neurons, where CaMKIIα expression is low, there is less segregation between AMPAR and NMDAR nanodomains. These neurons also exhibit smaller and fewer dendritic spines. Notably, overexpressing CaMKIIα in immature neurons alone was sufficient to recreate the mature synaptic landscape, characterized by the increased spine size and number, as well as greater segregation between these nanodomains. This effect of CaMKIIα could be abolished by a single CaMKIIα mutant

←

Mann–Whitney *U* test, $U = 3{,}561$) in GFP or GFP-CaMKIIα overexpressing neurons. ***G***, Distance between the center of AMPAR nanodomain to the center of the nearest NMDAR nanodomain (left, Mann–Whitney *U* test, $U = 7{,}151$) and distance between center of NMDAR nanodomain to the center of the nearest AMPAR nanodomain (right, Mann–Whitney *U* test, $U = 4{,}499$) in GFP and GFP-CaMKIIα overexpressing neurons. ***H***, Correlation between spine area and AMPAR/NMDAR overlapping ratio in GFP and GFP-CaMKIIα overexpressing neurons. AMPAR overlapping with NMDAR (left, Spearman's *R* test) and NMDAR overlapping with AMPAR (right, Spearman's *R* test) in GFP and GFP-CaMKIIα neurons. ***I***, The area of AMPAR (left, Mann–Whitney *U* test, $U = 6{,}692$) and NMDAR (right, Mann–Whitney *U* test, $U = 2{,}783$) nanodomains in GFP and GFP-CaMKIIα neurons. ***J***, Histogram of the number of AMPAR (left, Spearman's *R* test) and NMDAR (right, Spearman's *R* test) nanodomains per spine in GFP and GFP-CaMKIIα neurons. The same sets of spines are used in ***E*** to ***J***. $n = 102$ spines from 10 DIV10 GFP expressing neurons and 71 spines from 11 GFP-CaMKIIα expressing neurons, both at DIV10.

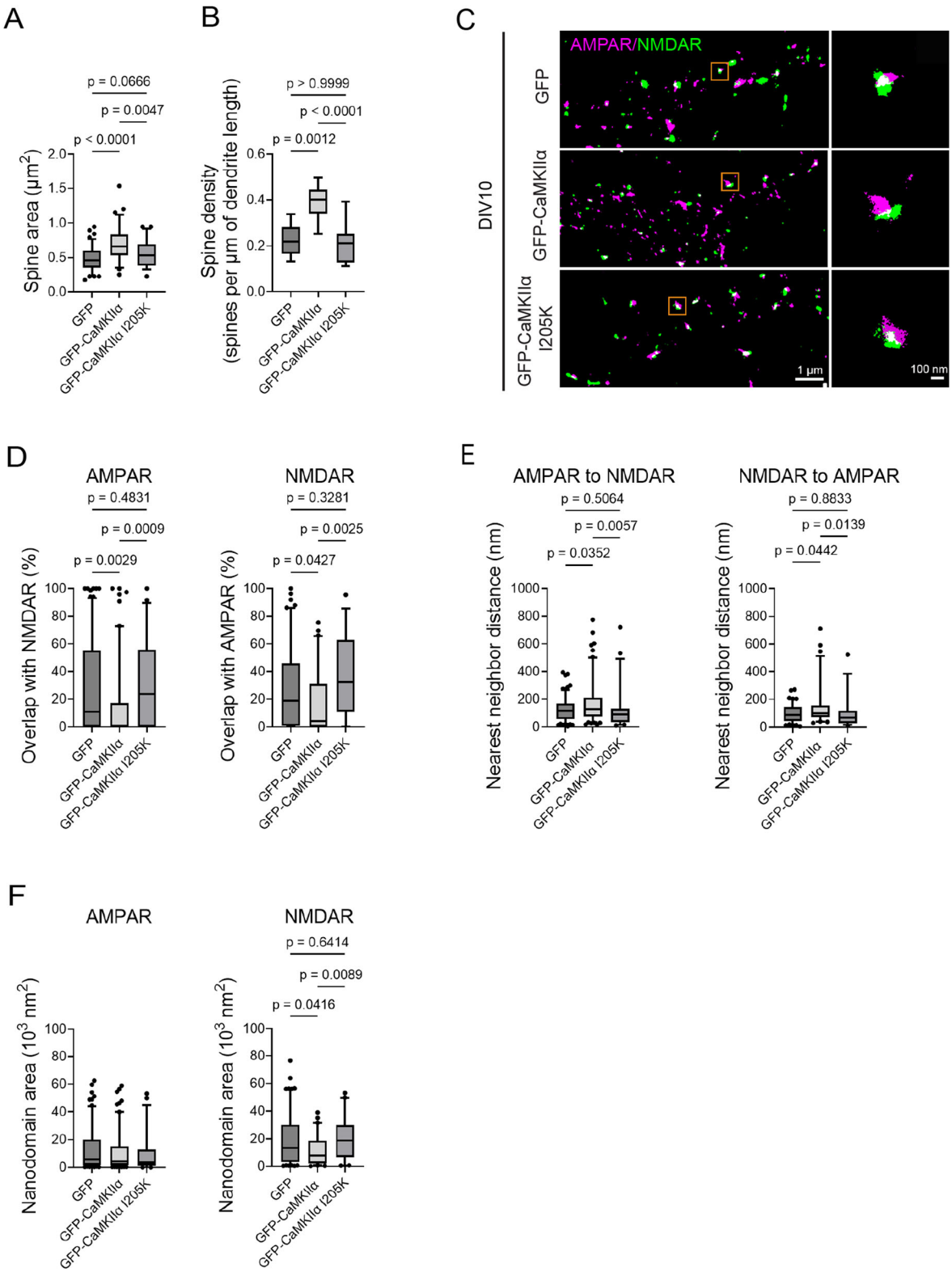

Figure 5. CaMKIIα I205K mutant disrupts LLPS and abolishes the effects of wild-type CaMKIIα overexpression. ***A***, Dendritic spine area in GFP, GFP-CaMKIIα, and GFP-CaMKIIα I205K overexpressing neurons (Kruskal–Wallis test, $H_{(2)} = 36.44$; $p < 0.0001$; Dunn's multiple-comparison test). $n = 85$ spines for GFP, 64 spines for GFP-CaMKIIα, and 51 spines for GFP-CaMKIIα I205K expressing neurons. ***B***, Dendritic spine density in GFP and GFP-CaMKIIα and GFP-CaMKIIα I205K overexpressing neurons (Kruskal–Wallis test, $H_{(2)} = 21.28$; $p < 0.0001$; Dunn's multiple-comparisons test). $n = 15$ neurons for GFP, 12 neurons for GFP-CaMKIIα, and 16 neurons for GFP-CaMKIIα I205K expressing neurons. ***C***, Merged dSTORM images of AMPAR and NMDAR nanodomains on the dendrite in GFP, GFP-CaMKIIα, and GFP-CaMKIIα I205K overexpressing DIV10 neurons (left). The orange box shows an example spine magnified on the right. White indicates the overlap between AMPAR and NMDAR. ***D***, Proportion of the AMPAR nanodomain area overlapping with the NMDAR nanodomain area (left, Kruskal–Wallis test, $H_{(2)} = 17.35$; $p = 0.0002$; Dunn's multiple-comparison test) and proportion of NMDAR nanodomain area overlapping with AMPAR nanodomain area (right, Kruskal–Wallis test, $H_{(2)} = 12.36$; $p = 0.0021$; Dunn's multiple-comparison test) in GFP, GFP-CaMKIIα, or GFP-CaMKIIα I205K overexpressing neurons. ***E***, Distance between the center of AMPAR nanodomain to the center of the nearest NMDAR nanodomain

that impairs LLPS. These findings suggest that the developmental increase in CaMKIIα, which could lead to increased CaMKIIα-mediated LLPS, plays a critical role in coordinating the promotion of both glutamate receptor organization and spine growth during synaptic maturation. Previous studies further support the notion that CaMKIIα promotes spine growth through mechanisms beyond its kinase activity. For instance, expression of the phospho-mimetic mutant T286D, which mimics the open, autonomously active form of CaMKIIα, was shown to increase spine density. Notably, the T286D/K42R double mutant, which mimics the open form while lacking kinase activity, produced a similar increase (Pi et al., 2010). Interestingly, the kinase-dead K42R mutant alone showed increased spine density at later developmental stages (e.g., DIV17), though not at earlier timepoints such as DIV9, suggesting that CaMKIIα kinase activity may not be essential for spine formation (Cornelia Koeberle et al., 2017). These findings suggest that autophosphorylated CaMKIIα, which helps maintain the open conformation that exposes the GluN2B interaction T-site, may play a more prominent role in promoting spine formation than its kinase activity.

These results are consistent with our proposal that CaMKIIα-mediated LLPS underlies coordinated structural and molecular remodeling at synapses. Specifically, in our previous study, we found that the exposure of the T-site and the autophosphorylation (T286) of CaMKIIα contribute to LLPS formation and maintenance, respectively (Hosokawa et al., 2021). Together with our findings, these prior observations underscore a model in which the structural state of CaMKIIα acts as a critical regulator of spine morphogenesis and receptor organization during development.

Our study, alongside previous research, suggests that synaptic proteins exhibit protein-specific developmental profiles. For instance, we observed that the nanodomain size of the AMPAR subunit GluA2 remained stable between DIV10 and DIV17, consistent with a previous study (Pickard et al., 2000). In contrast, the nanodomain size of the AMPAR subunit GluA1 increases during development (Sun et al., 2022).

For NMDARs, we observed a developmental decrease in the GluN1 nanodomain size, despite previous reports indicating that GluN1 surface expression levels remain constant (Pickard et al., 2000). This suggests that GluN1 nanodomains may become more concentrated over time, potentially driven by CaMKIIα-mediated LLPS. Conversely, prior studies have shown that the nanodomain sizes of NMDAR subunits GluN2A and GluN2B increase during development (Kellermayer et al., 2018). While these subunit-specific differences may arise from experimental variables—such as variations in targeted regions of interest (all synapses vs spine synapses), neuronal types (cortical vs hippocampal), or the analyzed cellular fraction (total vs surface AMPAR/NMDAR)—they likely also reflect subunit-specific developmental profiles. Although characterizing the behavior of individual synaptic proteins remains essential, it is equally important to consider the driving forces shaping overall synaptic nanoarchitecture. LLPS may represent a fundamental mechanism providing a unified explanation for the coordinated behaviors of synaptic proteins. LLPS could regulate receptor density at designated sites, control the size of receptor nanodomains, and govern receptor trafficking—powerful dials of synaptic transmission.

Synaptic maturation typically takes over 2 weeks for cultured neurons, suggesting that slow gradual, sequential steps are required. However, we demonstrated that critical aspects of mature synapses—such as greater AMPAR/NMDAR segregation, synaptic density, and spine size—can be recreated simply by overexpression of CaMKIIα in immature neurons. This suggests that by DIV10, many relevant factors are already present, and synapses are poised for maturation once CaMKII levels reach a threshold, acting like a switch to trigger their maturation.

CaMKII is well known for its dodecameric/tetradecameric structure (Yasuda et al., 2022), enabling it to serve as a signaling hub for multiple interacting partners. We identified that the interaction site between CaMKIIα and GluN2B, which is crucial for CaMKII-mediated LLPS, plays a key role in achieving mature AMPAR/NMDAR segregation and promoting spine growth. This suggests that LLPS drives the coordinated rearrangement of receptors and structural changes in spines needed for mature synaptic function. Such reorganization likely involves dynamic restructuring and recruitment of scaffolding and cytoskeletal proteins. Simultaneous imaging of these participants, along with advanced manipulation tools for LLPS, could help unveil this extensive remodeling of the synaptic nanoarchitecture which links spine growth and receptor segregation. As the presence of the trans-synaptic nanocolumn suggests, postsynaptic changes must be carefully coordinated with presynaptic changes. Whether CaMKII-mediated LLPS alone can align the presynaptic active zone with AMPARs for more effective glutamate sensing, thereby increasing the efficacy of synaptic transmission remains an exciting question for future research. Indeed, previous studies showed that overexpression of CaMKIIα in neurons at DIV10 increases the amplitude and decay time constant of AMPAR-mediated spontaneous EPSCs (Thiagarajan et al., 2002). The dynamic reorganization of synaptic proteins and spine remodeling is also crucial to our understanding of synaptic plasticity, also known to be triggered by the activation of CaMKII.

This study has certain limitations that also outline directions for future work. Although CaMKII expression was adjusted to approximate levels in mature neurons, overexpression systems may nonetheless introduce effects that differ from physiological conditions. The use of cultured hippocampal neurons provided a controllable system for mechanistic analysis, while acknowledging that the in vivo brain offers greater cellular diversity and network complexity that may shape outcomes differently. Similarly, although in vitro maturation models aspects of neuronal development, it cannot fully reproduce in vivo trajectories. Finally, we focused on the structural demonstration of LLPS-driven receptor segregation, and future studies will be needed to clarify how this organization impacts synaptic function.

←

(left, Kruskal–Wallis test, $H_{(2)} = 11.78$; $p = 0.0028$; Dunn's multiple-comparison test) and distance between center of NMDAR nanodomain to the center of the nearest AMPAR nanodomain (right, Kruskal–Wallis test, $H_{(2)} = 9.604$; $p = 0.0082$; Dunn's multiple-comparison test) in GFP, GFP-CaMKIIα, and GFP-CaMKIIα I205K overexpressing neurons. ***F***, The area of AMPAR (left, Kruskal–Wallis test, $H_{(2)} = 2.591$; $p = 0.2738$) and NMDAR (right, Kruskal–Wallis test, $H_{(2)} = 10.34$; $p = 0.0057$; Dunn's multiple-comparison test) nanodomains in GFP, GFP-CaMKIIα neurons, and GFP-CaMKIIα I205K overexpressing neurons. The same sets of spines are used in ***C*** to ***F***. $n = 85$ spines from 10 GFP expressing neurons and 68 spines from 9 GFP-CaMKIIα expressing neurons and 60 spines from 10 GFP-CaMKIIα I205K expressing neurons, all at DIV10.

References

Beghin A, Kechkar A, Butler C, Levet F, Cabillic M, Rossier O, Giannone G, Galland R, Choquet D, Sibarita J-B (2017) Localization-based super-resolution imaging meets high-content screening. Nat Methods 14:1184–1190.

Biederer T, Kaeser PS, Blanpied TA (2017) Transcellular nanoalignment of synaptic function. Neuron 96:680–696.

Cai Q, Zeng M, Wu X, Wu H, Zhan Y, Tian R, Zhang M (2021) CaMKIIα-driven, phosphatase-checked postsynaptic plasticity via phase separation. Cell Res 31:37–51.

Cornelia Koeberle S, Tanaka S, Kuriu T, Iwasaki H, Koeberle A, Schulz A, Helbing D-L, Yamagata Y, Morrison H, Okabe S (2017) Developmental stage-dependent regulation of spine formation by calcium-calmodulin-dependent protein kinase IIα and Rap1. Sci Rep 7:13409.

Fink CC, Bayer K-U, Myers JW, Ferrell JE, Schulman H, Meyer T (2003) Selective regulation of neurite extension and synapse formation by the β but not the α isoform of CaMKII. Neuron 39:283–297.

Hosokawa T, et al. (2021) CaMKII activation persistently segregates postsynaptic proteins via liquid phase separation. Nat Neurosci 24:777–785.

Hruska M, Henderson N, Le Marchand SJ, Jafri H, Dalva MB (2018) Synaptic nanomodules underlie the organization and plasticity of spine synapses. Nat Neurosci 21:671–682.

Kaech S, Banker G (2006) Culturing hippocampal neurons. Nat Protoc 1: 2406–2415.

Kechkar A, Nair D, Heilemann M, Choquet D, Sibarita J-B (2013) Real-time analysis and visualization for single-molecule based super-resolution microscopy. PLoS One 8:e62918.

Kellermayer B, et al. (2018) Differential nanoscale topography and functional role of GluN2-NMDA receptor subtypes at glutamatergic synapses. Neuron 100:106–119.e7.

Kelly PT, Shields S, Conway K, Yip R, Burgin K (1987) Developmental changes in calmodulin-kinase II activity at brain synaptic junctions: alterations in holoenzyme composition. J Neurochem 49:1927–1940.

Kim K, Saneyoshi T, Hosokawa T, Okamoto K, Hayashi Y (2016) Interplay of enzymatic and structural functions of CaMKII in long-term potentiation. J Neurochem 139:959–972.

Levet F, Hosy E, Kechkar A, Butler C, Beghin A, Choquet D, Sibarita J-B (2015) SR-Tesseler: a method to segment and quantify localization-based super-resolution microscopy data. Nat Methods 12:1065–1071.

Li A-J, Suzuki M, Suzuki S, Ikemoto M, Imamura T (2003) Differential phosphorylation at serine sites in glutamate receptor-1 within neonatal rat hippocampus. Neurosci Lett 341:41–44.

Liu P-W, Hosokawa T, Hayashi Y (2021) Regulation of synaptic nanodomain by liquid–liquid phase separation: a novel mechanism of synaptic plasticity. Curr Opin Neurobiol 69:84–92.

Martinez-Sanchez A, Laugks U, Kochovski Z, Papantoniou C, Zinzula L, Baumeister W, Lučić V (2021) Trans-synaptic assemblies link synaptic vesicles and neuroreceptors. Sci Adv 7:eabe6204.

Özden C, et al. (2022) CaMKII binds both substrates and activators at the active site. Cell Rep 40:111064.

Papa M, Bundman MC, Greenberger V, Segal M (1995) Morphological analysis of dendritic spine development in primary cultures of hippocampal neurons. J Neurosci 15:1–11.

Pi HJ, Otmakhov N, El Gaamouch F, Lemelin D, De Koninck P, Lisman J (2010) CaMKII control of spine size and synaptic strength: role of phosphorylation states and nonenzymatic action. Proc Natl Acad Sci U S A 107:14437–14442.

Pickard L, Noël J, Henley JM, Collingridge GL, Molnar E (2000) Developmental changes in synaptic AMPA and NMDA receptor distribution and AMPA receptor subunit composition in living hippocampal neurons. J Neurosci 20:7922–7931.

Sun S-Y, Li X-W, Cao R, Zhao Y, Sheng N, Tang A-H (2022) Correlative assembly of subsynaptic nanoscale organizations during development. Front Synaptic Neurosci 14:748184.

Tang A-H, Chen H, Li TP, Metzbower SR, MacGillavry HD, Blanpied TA (2016) A trans-synaptic nanocolumn aligns neurotransmitter release to receptors. Nature 536:210–214.

Thiagarajan TC, Piedras-Renteria ES, Tsien RW (2002) α- and βCaMKII. Inverse regulation by neuronal activity and opposing effects on synaptic strength. Neuron 36:1103–1114.

Yasuda R, Hayashi Y, Hell JW (2022) CaMKII: a central molecular organizer of synaptic plasticity, learning and memory. Nat Rev Neurosci 23:666–682.